JOURNAL OF COMPUTATIONAL PHYSICS 69, 81–111 (1987)

Finite Element Simulation of Planar Instabilities during Solidification of an Undercooled Melt

JOHN M. SULLIVAN, JR., AND DANIEL R. LYNCH

Thayer School of Engineering, Dartmouth College, Hanover, New Hampshire 03755

AND

KEVIN O'NEILL

U.S. Army Cold Regions Research and Engineering Laboratory, Hanover, New Hampshire

Received November 8, 1985; revised May 2, 1986

Two-dimensional finite element solutions for planar solidification from an undercooled melt are presented. These simulations are based on the transient heat equation in both solid and liquid and show the onset and propagation of both stable and unstable numerical waveforms which reproduce those predicted in the continuum analysis with fidelity. The inherent instabilities associated with the freezing process dictate a more comprehensive treatment of the interfacial temperature than that specified in stable Stefan-type problems. Herein, we apply radiation-type boundary conditions on the interface that incorporate temperature effects associated with curvature and interfacial kinetics. The interfacial temperature depression due to curvature is the primary restraining factor during dendritic growth. Its numerical representation requires special care to avoid fatal discretization error; additionally, curvature must be treated implicitly within the thermal iteration and within the time step to overcome otherwise severe time-step constraints. The numeric simulations of anisotropic ice show similar waveform patterns at the onset of the instability to those of isotropic cases. However, as the amplitude of the waveform increases significant lengths of interface become orientated along the C axis where interfacial kinetics inhibit growth. This alters the interface shape by elongating the dendrite finger.

INTRODUCTION

Dendritic growth of crystals into an undercooled melt is the most common form of solidification. Any protuberance or bump on a planar solid/liquid interface that extends itself into the melt enhances its growth since the surrounding temperature gradient is greater than that about the planar surface. Consequently, the bump accelerates its growth relative to the planar front until it is constrained by such factors as surface energy. Several stability analyses have been developed that attempt to characterize the growth of these perturbations as a function of solidification parameters [1–3]. Briefly, the factors of significance and their effect on solidification are:

0021-9991/87 $3.00

Undercooling of the bulk fluid. Increasing the level of undercooling enhances the transfer of heat away from the interface.

Solute concentration. Solute displaced ahead of the freezing front lowers the thermodynamic equilibrium freezing temperature. This mitigates the undercooling effect in the zone of higher solute concentration.

Geometry. The geometry of a dendrite tip is observed to resemble a paraboloid of revolution for isotropic materials or a parabolic cylinder in the case of ice, an anisotropic material. For the undercooling range of interest curvature is measured in microns at the parabola tip which causes a local temperature depression due to interfacial surface energy effects. This curvature effect results in a geometry dependent temperature distribution along the dendrite tip.

Interfacial growth kinetics. Anisotropic materials such as ice have significant interfacial kinetic differences between growth planes. This molecular deposition variation contributes to the temperature variation along the crystal surface.

In an earlier work [4] we examined and compared to available analytic solutions the effects of interfacial kinetics and solute concentration for one-dimensional finite element simulations of solidification from an undercooled solution. Herein, we address two-dimensional formulations of the above problem in quiescent fluid without solutes, to focus on the unstable geometrical evolution and its representation on finite elements. The numerical treatment of curvature emerges as a key ingredient for successful simulation of the physical instability.

Problem Statement

Consider a solidification situation consisting of two quiescent phases separated by an interface, S, as in Fig. 1. By convention, the normal vector on S is directed

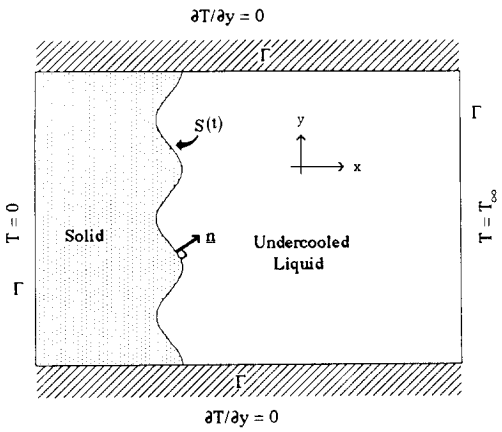

FIG. 1. Two-phase domain with interface S.

into the melt. The solidification problem consists of the heat equation on both phases separately:

$$c\frac{\partial T}{\partial t} - K\nabla^2 T = 0, \tag{1}$$

where the heat capacity and thermal conductivity K are assumed constant within each domain. The usual boundary conditions apply on Γ and are given in Fig. 1. However, temperature and velocity interface conditions are required on S.

If the only factor affecting the solidification rate were undercooling of the bulk fluid, the system could be treated as a Stefan problem with the interface temperature, T_S, equal to the thermodynamic temperature for a planar front with no solute, T_m. However, since solute concentration, geometry and interfacial kinetics contribute to the growth mechanism, the interface temperature is variable:

$$T_s(x, y) = T_m - T_c - T_r - T_k, \tag{2a}$$

where the solute concentration effect $T_c = 0$ for a pure melt and T_r is the curvature effect due to geometry based on the Gibbs–Thomson relation

$$T_r = (\gamma T_m/L)\,\mathbb{C} = (\gamma T_m/L)(1/r_1 + 1/r_2) \tag{2b}$$

with L being the volumetric latent heat of fusion and γ the interfacial energy. The curvature $\mathbb{C}$ is the reciprocal of the principle radii, r_1 and r_2 and is assumed positive for a concave solid, i.e., when the curvature center is located within the solid. The interfacial kinetic effect has been expressed as [5]:

$$T_k = (\mathbf{V}\cdot\underline{\mathbf{n}})/\mu, \tag{2c}$$

where $\mathbf{V}\cdot\underline{\mathbf{n}}$ is the normal component of the phase front velocity with $\underline{\mathbf{n}}$ being the unit normal vector and μ is the kinetic mobility factor. Substituting (2b) and (2c) into (2a) and rearranging gives an expression for the equation of motion;

$$\mathbf{V}\cdot\underline{\mathbf{n}} = \mu[-(\gamma T_m/L)\,\mathbb{C} - T], \tag{2d}$$

where T is the temperature expressed as a deviation from T_m, i.e., $T = (T_S - T_m)$.

The velocity boundary condition at the phase front must preserve the balance between the system's ability to transport sensible heat away from the interface and the latent heat of fusion released during solidification, i.e.,

$$L\mathbf{V}\cdot\underline{\mathbf{n}} = \Delta(K\nabla T)\cdot\underline{\mathbf{n}} \tag{3}$$

where $\Delta(K\nabla T)\cdot\underline{\mathbf{n}}$ is the jump in heat flux across the interface. Here the densities of the two phases are assumed equal.

For many isotropic materials the kinetic mobility factor is assumed sufficiently large that T_k vanishes and the boundary temperature is effectively uncoupled from the velocity. However, retaining (2d) with finite μ enables us to model the

solidification of water, an anisotropic material of primary physical importance whose kinetic mobility ranges from near zero in the C axis to an effective value of infinity in the A axis.

Numerical Formulation

Our starting point is the Galerkin formulation of the heat equation on deforming elements as articulated previously [6–10];

$$\langle c(dT/dt)\,\Phi_i - c\mathbf{V}\cdot\nabla T\Phi_i + K\nabla T\cdot\nabla\Phi_i\rangle = \int_\Gamma K\nabla T\cdot\underline{\mathbf{n}}\Phi_i d\Gamma + \int_s L\mathbf{V}\cdot\underline{\mathbf{n}}\Phi_i dS, \tag{4}$$

where $\langle(\,)\rangle$ is the inner product notation representing the sum of integrations over both phases together; Φ_i are the finite element bases, and $\mathbf{V}$ is the velocity of the mesh. Formulation of the problem in this manner means that it is solved directly in a moving coordinate system. The nodes initially on S continually track the phase boundary, and the latent heat balance (3) has been utilized in the surface integral on S.

We substitute (2d) into the phase boundary integral and separate the effects of curvature and temperature:

$$\int_s L\mathbf{V}\cdot\underline{\mathbf{n}}\Phi_i dS = -\int_s \mu\gamma T_m\mathbb{C}\Phi_i dS - \int_s L\mu T\Phi_i dS \tag{5}$$

The temperature component of the surface integral is treated in similar fashion to our one-dimensional investigations where curvature was not an issue [4];

$$\int_s L\mu T\Phi_i dS = LT_j\int_s \mu\Phi_j\Phi_i dS, \tag{6}$$

where a repeated index implies summation over that index. In the continuum curvature is by definition the change in angle with respect to arc length, $d\alpha/ds$ in Fig. 2a. The curvature portion of (5) can be written as:

$$\int_s \mu\gamma T_m\mathbb{C}\Phi_i dS = \int_s \mu\gamma T_m\Phi_i d\alpha \tag{7}$$

which we evaluate on the actual finite element geometry. On the simple linear elements in use here, $d\alpha$ is zero except at the nodes, Fig. 2b. Hence, (7) is easily evaluated:

$$\int_s \mu\gamma T_m\mathbb{C}\Phi_i dS = \mu\gamma T_m\Delta\alpha_i. \tag{8}$$

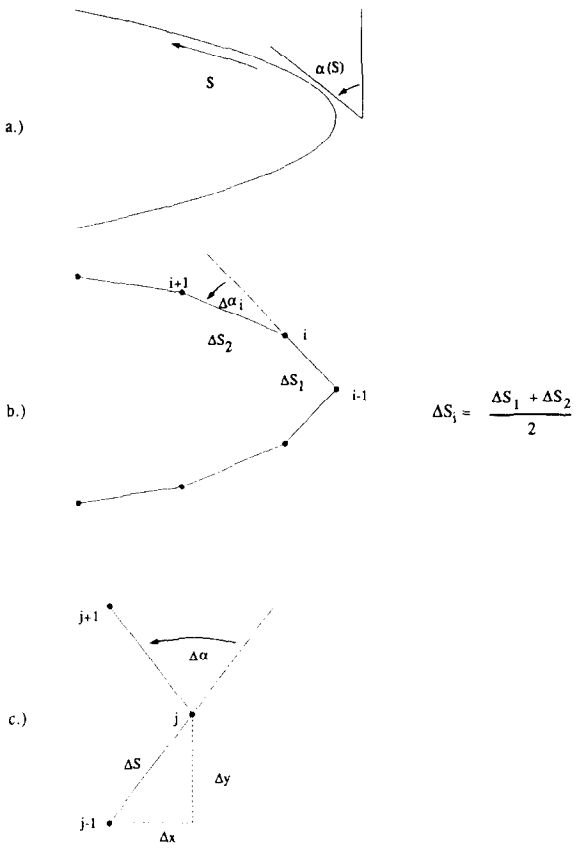

FIG. 2. (a) Curvature in the continuum, $\mathbb{C}(s) = d\alpha/ds$. (b) Curvature treatment on a discretized boundary. (c) Example of symmetric phase boundary discretization.

In effect, we have generated a difference expression for curvature $\mathbb{C}_i = (\Delta\alpha/\Delta S)_i$ with $\Delta S_i = \int_s \Phi_i dS$ as indicated in Fig. 2b. Reassembling the surface integral in (4) produces the final Galerkin formulation;

$$\langle c(dT/dt)\,\Phi_i - c\mathbf{V}\cdot\nabla T\Phi_i + K\nabla T\cdot\nabla\Phi_i\rangle$$

$$= \int_{\Gamma} K\nabla T\cdot\underline{\mathbf{n}}\Phi_i d\Gamma - L\int_s \mu T\Phi_i dS - \mu\gamma T_m \Delta\alpha_i. \tag{9}$$

CURVATURE

A. *Resolution*

Curvature is the primary restraining factor in the otherwise physically unstable situation of solidification from an undercooled melt [3]. Consider the discretized phase front in Fig. 2c and let node j have an x-velocity greater than that of its

neighbors. Initially, the numeric curvature grows, but as ΔS approaches ∞ the numeric curvature decays back to zero. Alternately, let $\Delta\alpha$ approach its maximum value of π for node j with ΔS constant. The calculated curvature remains finite as opposed to a value approaching ∞ in the continuum. Consequently, for some minimum level of undercooling the numeric curvature is insufficient to properly constrain a protuberance or bump on the phase front and the perturbation amplitude grows without bound.

Figure 3 compares numeric and analytic values of curvature as a function of $\Delta\alpha$ for a dendrite tip symmetric about the x-axis as in Fig. 2c, with Δy constant. The analytic curvature is taken as that of a parabola fit to the 3 points, $\mathbb{C}_A = 2\Delta x/\Delta y^2$. The maximum numeric curvature occurs at $\Delta\alpha^* = 98.6°$, where the condition is

$$\mathrm{Cot}(\Delta\alpha/2) = \Delta\alpha/2. \tag{10}$$

Of course, maintaining $\Delta\alpha < \Delta\alpha^*$ is far from sufficient for accuracy purposes when compared to $\mathbb{C}_A$. For a 95% accurate representation of curvature $\Delta\alpha \leqslant \Delta\alpha^{**} \sim 28.2°$ by evaluation, Fig. 3. This analysis suggests that the numerical system would at least remain stable if $\Delta\alpha$ were kept below roughly 90°.

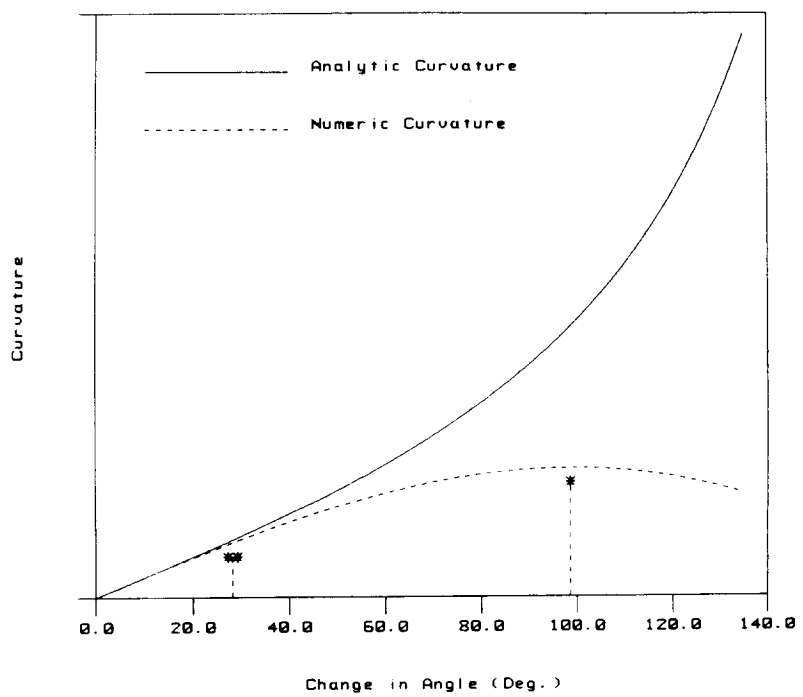

FIG. 3. Analytic curvature of a parabola fit to 3 points versus numeric curvature as a function of $\Delta\alpha$. The maximum numeric curvature occurs at $\Delta\alpha^* = 98.6°$. To retain 95% accuracy, $\Delta\alpha \leqslant \Delta\alpha^{**} = 28.2°$.

B. *Dynamics*

To isolate the dynamics of geometric perturbations, consider only the relations:

$$(\mathbf{V}\cdot\underline{\mathbf{n}})_i = -\mu(\gamma T_m/L)\,\mathbb{C}_i + F_i, \tag{11}$$

where the driving forces F_i are known. These are to be solved on a grid as in Fig. 4 in which the mesh velocity in the y direction is set to zero for all nodes. Thus, $\mathbf{V}\cdot\underline{\mathbf{n}} = V_x \cos\alpha$ and (11) is expressed as

$$(\cos\alpha_i)\,dx_i/dt = (\mathbf{V}\cdot\underline{\mathbf{n}})_i = [-\mu(\gamma T_m/L)\,\mathbb{C}_i + F_i]. \tag{12}$$

Assume there is a steady solution $x_i^{\circ}(t)$ such that all node velocities are the same ($= V_0$ in the x direction); and that a perturbation $\varepsilon_i(t)$ is introduced:

$$x_i(t) = x_i^{\circ}(t) + \varepsilon_i(t). \tag{13}$$

Substituting into (12) and linearizing about $x_i^{\circ}(t)$ yields:

$$\cos\alpha_i[d\varepsilon_i/dt] + V_0\varepsilon_j\hat{c}\cos\alpha_i/\hat{c}x_j = -\mu(\gamma T_m/L)(\hat{c}\mathbb{C}_i/\hat{c}x_j)\,\varepsilon_j. \tag{14}$$

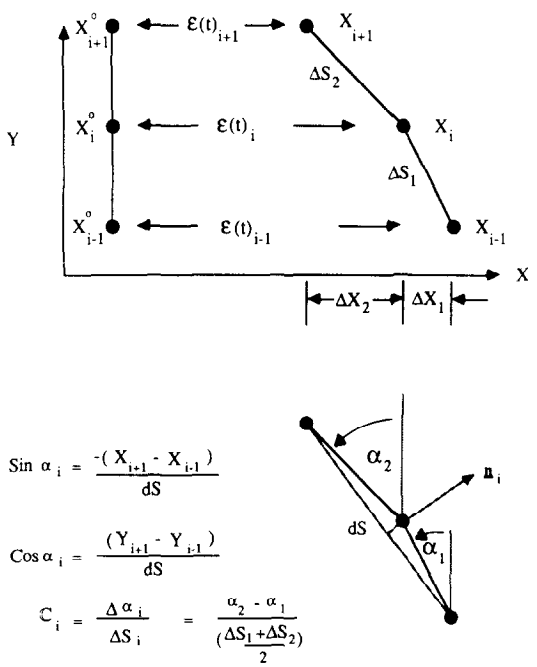

FIG. 4. Grid used for analysis of curvature dynamics with small perturbation ε.

The derivatives of curvature are

$$\partial \mathbb{C}_i/\partial x_{i-1} = -\cos\alpha_1/(\Delta S_i \Delta S_1) - \mathbb{C}_i \sin\alpha_1/(2\Delta S_i), \tag{15a}$$

$$\partial \mathbb{C}_i/\partial x_i = [\cos\alpha_1/\Delta S_1 + \cos\alpha_2/\Delta S_2]/\Delta S_i - \mathbb{C}_i[\sin\alpha_2 - \sin\alpha_1]/(2\Delta S_i), \tag{15b}$$

$$\partial \mathbb{C}_i/\partial x_{i+1} = -\cos\alpha_2/(\Delta S_i \Delta S_2) + \mathbb{C}_i \sin\alpha_2/(2\Delta S_i), \tag{15c}$$

and similarly for $\cos\alpha_i$;

$$\partial \cos\alpha_i/\partial x_{i-1} = -\cos\alpha_i \sin\alpha_i/ds, \tag{16a}$$

$$\partial \cos\alpha_i/\partial x_i = 0, \tag{16b}$$

$$\partial \cos\alpha_i/\partial x_{i+1} = +\cos\alpha_i \sin\alpha_i/ds, \tag{16c}$$

and upon substitution into (14) we find:

$$\cos\alpha_i\left[\frac{d\varepsilon_i}{dt} + V_0\frac{\sin\alpha_i}{ds}(\varepsilon_{i+1} - \varepsilon_{i-1})\right]$$
$$= \frac{\mu\gamma T_m}{L\Delta S_i}\left[\frac{\cos\alpha_2}{\Delta S_2}(\varepsilon_{i+1} - \varepsilon_i) - \frac{\cos\alpha_1}{\Delta S_1}(\varepsilon_i - \varepsilon_{i-1})\right]$$
$$- \frac{\mu\gamma T_m}{2L\Delta S_i}\mathbb{C}_i[\sin\alpha_2(\varepsilon_{i+1} - \varepsilon_i) + \sin\alpha_1(\varepsilon_i - \varepsilon_{i-1})]. \tag{17}$$

Equation (17) is readily identified as a difference approximation to the advective–diffusive equation;

$$\cos\alpha\left[\frac{d\varepsilon}{dt} + V_0\sin\alpha\frac{\partial\varepsilon}{\partial s}\right] = \frac{\mu\gamma T_m}{L}\left[\frac{\partial}{\partial s}\left(\cos\alpha\frac{\partial\varepsilon}{\partial s}\right) - \mathbb{C}\sin\alpha\frac{\partial\varepsilon}{\partial s}\right], \tag{18}$$

where the material derivative $d(\ )/dt$ reflects the fact that nodes are in motion along S,

$$\frac{d\varepsilon}{dt} = \frac{\partial\varepsilon}{\partial t} + V_S\frac{\partial\varepsilon}{\partial s}. \tag{19}$$

Since $V_S = -V_0\sin\alpha$, we have in (17) a deforming-grid treatment of

$$\frac{\partial\varepsilon}{\partial t} + \frac{\mu\gamma T_m}{L}\mathbb{C}\tan\alpha\frac{\partial\varepsilon}{\partial s} = \frac{\mu\gamma T_m}{L\cos\alpha}\frac{\partial}{\partial s}\left(\cos\alpha\frac{\partial\varepsilon}{\partial s}\right). \tag{20}$$

Evidently perturbations on a plane front or at a dendrite tip are basically diffusive, while advection gains significance due to both mesh motion and curvature as one moves downstream from a dendrite tip. In either case one may expect the usual parasitic behavior to emerge from roundoff error at small wavelengths relative to ΔS. Control of these parasites is essential to successful simulation and dimensionless

groups analogous to the Fourier, Courant, mesh Courant and Peclet numbers may be identified:

$$Fo = \mu(\gamma T_m/L)\,\Delta t/\Delta S^2 = \sigma, \tag{21}$$

$$Co = \mu(\gamma T_m/L)\,\mathbb{C}\tan\alpha\Delta t/\Delta S = \sigma\Delta\alpha\tan\alpha, \tag{22}$$

$$Cm = V_0 \sin\alpha\Delta t/\Delta S, \tag{23}$$

$$Pe = \mathbb{C}\tan\alpha\Delta S = \Delta\alpha\tan\alpha. \tag{24}$$

Consider a conventional two-level time-stepping scheme, with time levels superscripted

$$(x_i^{k+1} - x_i^k)/\Delta t = f[\theta\mathbb{C}_i^{k+1} + (1-\theta)\,\mathbb{C}_i^k]. \tag{25}$$

From the above analysis, a plane front may be expected to be unstable for $\theta < \frac{1}{2}$ unless

$$\sigma < 1/[2(1-2\theta)] \tag{26}$$

based on the Von Neumann stability analysis [11].

Next consider an explicit iterative approach to making (25) implicit in time

$$[(x^{k+1})^{m+1} - x^k]_i = f[\theta(\mathbb{C}_i^{k+1})^m + (1-\theta)\,\mathbb{C}_i^k]\,\Delta t. \tag{27}$$

Here m is an iteration counter and the unknown $\mathbb{C}^{k+1}$ is simply lagged. The constraint on σ returns in different form—in this case for iterative stability [11],

$$\sigma < 1/(4\theta), \tag{28}$$

is required even for $\theta \geqslant \frac{1}{2}$. The two constraints (26) and (28) are plotted in Fig. 5. It is clear that $\sigma = 1$ is the absolute upper limit which can be achieved without implicit computation of curvature within the iteration.

The severity of this time-step constraint is disastrous. Consider modeling the freezing of water from a 1°C undercooled melt. The radius of curvature for the dendrite tip is $R \sim 0.6 \times 10^{-4}$ cm, Ref. [12]. Using the maximum node spacing ($\Delta\alpha = \Delta\alpha^*$) gives $\Delta S \sim 3.6R$ or a time-step constraint of $\Delta t \leqslant 1.8 \times 10^{-3}s$. Modeling the ice crystal for a node spacing with $\Delta\alpha = \Delta\alpha^{**}$ requires 25,000 time steps to stimulate one second of crystal growth!

Our numerical experiments have shown these constraints to be reliable. As a result we conclude that the contribution of curvature to boundary motion must be treated implicitly in time *and* within the iteration required during each time step. Effectively, the impact of $\mathbf{V}_{i+1}$ on $\mathbb{C}_i$, and therefore on $\mathbf{V}_i$, must be present in the calculation without delay.

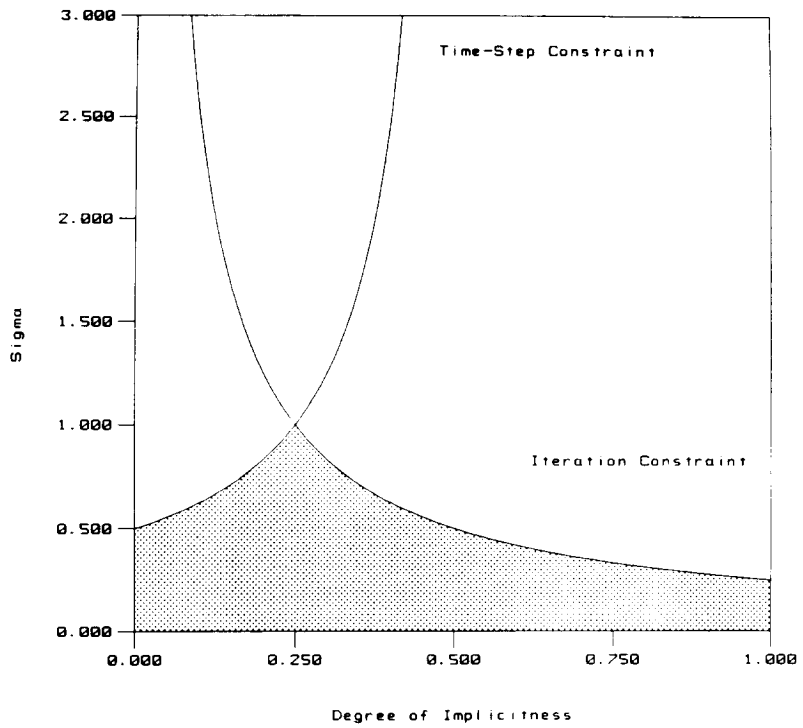

FIG. 5. Sigma constraint is unavoidable when $\mathbb{C}$ is treated explicitly in either the time step or the iteration within the time step.

SOLUTION STRATEGY

In the simulations shown below, node motion is managed as follows. On S, $\mathbf{V} \cdot \underline{\mathbf{n}}$ is specified by equations (2d) and (3) but the tangential motion is arbitrary. For convenience we set $V_y = 0$ and thus $V_x = \mathbf{V} \cdot \underline{\mathbf{n}}/(\underline{\mathbf{x}} \cdot \underline{\mathbf{n}})$, where $\underline{\mathbf{x}}$ is the unit vector in the x direction and $\underline{\mathbf{x}} \cdot \underline{\mathbf{n}} = \cos \alpha$. This simple strategy suffices for the present purpose of simulating unstable waves on a planar front, but prohibits the development of sidebranching and other shapes where x is not a single-valued function of y. This matter is taken up again in the discussion of simulation results.

Interior node motion is interpolated by a Laplace operator on the current mesh geometry, with $V_y = 0$ everywhere.

The algebraic system is nonlinear and solved iteratively. Three solution strategies of increasing complexity are delineated that successfully solve the following two-phase solidification situations, respectively;

(a) two-dimensional, stable Stefan-type solidification with isothermal interface,

(b) one-dimensional, undercooled solidification with interfacial kinetics, and

TABLE I

Flow Chart for Solution of Two-Dimensional, Stable Stefan-Type Solidification with Isothermal Interface

Initialize System
- *Time Stepping Loop* – Index k
  - *Iteration Loop* – Index m
    - $\{(x, y)\}_i^{(k+\theta)^m} = \{(x, y)\}_i^k + \theta \Delta t \{\mathbf{V}\}_i^m$
    - Solve interior node motion using a Laplace operator on mesh at time level k
    - Construct left-hand side of (4)
    - Apply boundary conditions on Γ according to Fig. 1
    - Apply type I boundary conditions on S
    - Solve for $\{T^{k+1}\}_i^{m+1}$ for interior nodes and solve for $\int_S L\mathbf{V} \cdot \mathbf{n}\Phi_i dS$ on the phase boundary.
    - Calculate V_N^{m+1} from $\int_S L\mathbf{V} \cdot \mathbf{n}\Phi_i dS$
    - Convergence $\|1 - (V^{m+1}/V^m)_i^{k+1}\| \leqslant 10^{-4}$ for nodes on S
  - $m = m + 1$ — No
  - Yes → Update arrays $k = k + 1$
- No — Time limit reached
- Yes → Terminate Program

TABLE II

Flow Chart for Solution of One-Dimensional Solidification with Interfacial Kinetics

Initialize System
- *Time Stepping Loop* – Index k
  - *Iteration Loop* – Index m
    - $\{T\}^{(k+\theta)^m} = \theta\{T\}^{(k+1)^m} + (1-\theta)\{T\}^k$
    - $\{V\}^m = -\mu\{T\}^{(k+\theta)^m}$
    - $\{x\}^{(k+\theta)^m} = \{x\}^k + \theta \Delta t \{V\}^m$
    - Solve interior node motion using a $1-D$ stretching routine
    - Construct left-hand side of (4)
    - Apply type I boundary conditions at $x = 0$ and $x = \infty$
    - Apply type III boundary condition on node N using (29)
    - Solve for $\{T^{k+1}\}_i^{m+1}$
    - Convergence $\|1 - (T^{m+1}/T^m)_N^{k+1}\| \leqslant 10^{-4}$ where N is the phase boundary node
  - $m = m + 1$ — No
  - Yes → Update arrays $k = k + 1$
- No — Time limit reached
- Yes → Terminate Program

(c) two-dimensional, unstable solidification with interfacial kinetics and curvature.

For stable Stefan solidification problems our solution strategy follows Table I. The phase-front velocities are initially obtained from the previous time step or initial conditions. These velocities are used to position the grid at time $t^{k+\theta}$ and they are used in the advection term of (4). Type I boundary conditions are applied along the phase front since the interface is isothermal. Consequently, solution of (4) yields the velocity boundary condition integrated over S in a heat conserving manner [9]. This result provides new phase front velocity estimates and the calculations are repeated until convergence is reached during the time step.

The one-dimensional, undercooled solidification routine [4] modified the above strategy, Table II. The phase front velocity is obtained from (2d) with $\mathbb{C} = 0$. In this system the phase front is not necessarily isothermal and type III boundary conditions are applied on the phase front. The surface integral in (4) reduces to its 1-D version:[1]

$$L\mathbf{V}\cdot\underline{\mathbf{n}}\Phi_N\big|_S^{(k+\theta)^{m-1}} = -\mu L T_N^{(k+\theta)^{m-1}} = LV_N^m - \mu L\theta(T^{m+1}-T^m)_N^{k+1} \tag{29}$$

for interface node N. The new phase front temperature estimate $(T_N^{m+1})^{k+1}$ from solution of (4) is then used in (2d) to update the velocity estimate for the next iteration. As in the stability analysis presented for curvature previously, T^{k+1} cannot be simply lagged in the iteration without incurring a time-step constraint based on $\Delta t\mu L/(c\,\Delta x)$, which is prohibitive.

The 2-D solidification of undercooled melts introduces the additional complication of curvature. Solution of this nonlinear algebraic system is flow charted in Table III. The phase front velocities are obtained from (2d) where $\mathbb{C}$ is evaluated at time $t^{k+\theta}$ by expanding $\mathbb{C}$ about its previous iteration estimate, i.e.,

$$\mathbb{C}_i^{(k+\theta)^m} = \mathbb{C}_i^{(k+\theta)^{m-1}} + \frac{\partial \mathbb{C}_i^{(k+\theta)^{m-1}}}{\partial x_j}\,\theta(x^m - x^{m-1})_j^{k+1}. \tag{30}$$

A tridiagonal system involving phase boundary nodes is required to solve for the position update $\delta_i = (X^m - X^{m-1})_i^{k+1}$ in the velocity equation

$$\delta_i + \Delta t V_i^{m-1} + \Delta t(\mu/\cos\alpha_i)(\gamma T_m/L)\left\{\mathbb{C}_i^{(k+\theta)^{m-1}} + \frac{\partial \mathbb{C}_i^{(k+\theta)^{m-1}}}{\partial x_j}\,\theta\delta_j\right\} + (\Delta t\mu/\cos\alpha_i)\,T_i^{(k+\theta)^m} = 0 \tag{31}$$

which produces the velocity estimate V_i^m ($= \delta_i/\Delta t + V_i^{m-1}$). V^m are used to position

[1] Superscript m indicates iteration level; k indicates time level.

TABLE III

Flow Chart for Solution of Two-Dimensional, Unstable Solidification with Interfacial Kinetics and Curvature

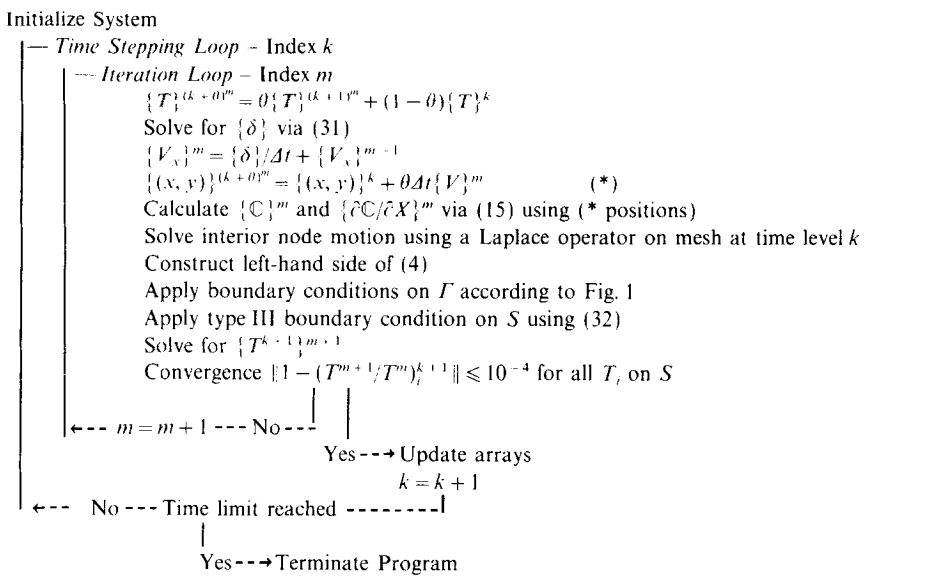

the grid at time $k+\theta$ and in the advection term of (4), and calculation of T^{m+1} is begun via (4). The surface integral in (4) is the 2-D representation of (29);

$$\int_S L\mathbf{V}\cdot\underline{\mathbf{n}}\Phi_i dS = \int_S L(\mathbf{V}\cdot\underline{\mathbf{n}})^m \Phi_i dS - \int_S \mu L\theta(T^{m+1}-T^m)^{k+1}\Phi_i dS, \tag{32}$$

where T and $\mathbb{C}$ are treated implicitly. As in the 1-D case, the new phase front temperature solution from (4) is used in (31) for the next velocity updates and the calculation is repeated to convergence. The numeric results presented typically required 15 iterations within each time step during early periods of the simulation. Once the dominant waveform surfaced the iteration count dropped to 5.

Planar Stability Analysis

Mullins and Sekerka [1] and later Langer [3] have provided excellent steady-state, linear stability analyses for a planar front solidifying from a pure undercooled melt, and we use this to verify our numerical method. The kinetic attachment mechanism is assumed to be rapid such that (2) reduces to:

$$T = -(\gamma T_m/L)\,\mathbb{C}. \tag{33}$$

Following Langer [3], a small perturbation $\zeta(y, t) = \zeta_0 \exp(iky + \omega t)$ is imposed on the interface where k is the wavenumber and ω is the amplification rate. For $\omega > 0$ the perturbation grows with time and the system becomes unstable. A similar perturbation $T_0 \exp(iky - qx + \omega t)$ is imposed on the temperature field. Application of the heat equation yields

$$q^L = (V/2D) + \sqrt{[(V/2D)^2 + (k^2 + \omega/D)]}, \tag{34a}$$

$$q^S = (V/2D) - \sqrt{[(V/2D)^2 + (k^2 + \omega/D)]}, \tag{34b}$$

where we have retained the transient term ω/D with D being the thermal diffusivity. Application of the boundary conditions on temperature and latent heat then yields the amplification rate (Eq. (3.14) in Ref. [3]):

$$\omega = V[q^L - V/D] - d_0 k^2 D[q^L - \beta q^S], \tag{35}$$

where d_0 is the capillary length, $(\gamma T_m/L)(c/L)$, and β is the solid–liquid thermal conductivity ratio. While in [3] this relation is obtained for a steady state, unit undercooling situation, we find that these assumptions are not necessary, and that

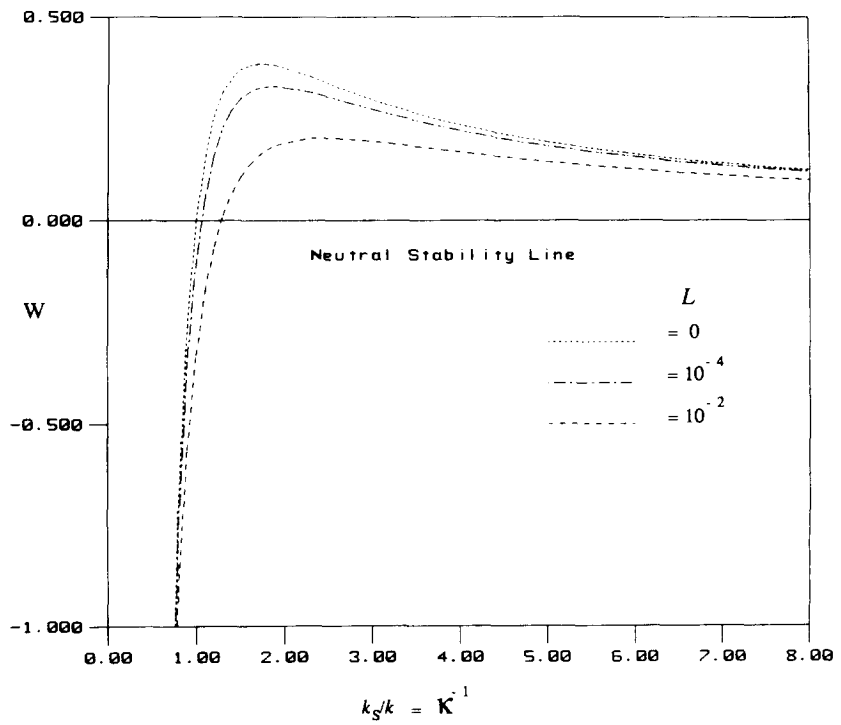

FIG. 6. Nondimensional amplification factor $W = \omega(Vk_s)$ as an inverse function of nondimensional wavenumber $\kappa = k/k_s$ for capillary–diffusion ratios of $L = 10^{-2}$, 10^{-4}, and the limiting case of $L = 0$.

(35) may be derived even when the background solution is transient (see Appendix).

The majority of our numerical results are for Succinonitrile such that $\beta \sim 1$. Simplifying (35) and nondimensionalizing ω with k_s, the critical (neutral stability) wavenumber for $\mathscr{P} = 0$, gives

$$W = (1 - \kappa^2)\sqrt{[\mathscr{P}^2 + \kappa^2 + 2W\mathscr{P}]} - \mathscr{P}, \tag{36}$$

where $W = \omega/(Vk_s)$, $\kappa = k/k_s$, $\mathscr{P} = \sqrt{d_0}/\sqrt{l_d}$, $l_d = 2D/V$ and $k_s = 1/\sqrt{(d_0 l_d)}$. In Fig. 6 we plot in nondimensional form the amplification factor as a function of wavenumber for various capillary–diffusion length ratios. Note that for typical values of $\mathscr{P} \sim 10^{-6}$ the amplification factor peaks at 0.38 and the fastest growing wave corresponds to that predicted by Langer [3], ($\kappa = 1/\sqrt{3}$).

Below we seek to demonstrate the qualitative and quantitative reproduction of the main features of Fig. 6, including a critical wavenumber, k_s, separating long unstable waves from short stable ones; and a maximum growth wave at roughly $(1/\sqrt{3})k_s$ which dominates in long-term simulation. We quantify the observed amplification rate by integrating the identity $\omega\zeta = \partial\zeta/\partial t$;

$$\omega = \Delta \ln(\zeta)/\Delta t. \tag{37}$$

If one carries the analysis beyond its small-amplitude assumptions it is possible to predict the point at which the front velocity in "valleys" (negative $\mathbb{C}$) will become negative:

$$V + \omega\zeta = 0. \tag{38}$$

Assuming $\mathscr{P}$ is small, we have $\omega = 0.38Vk_s$ and $k_s = \sqrt{3}k$, then solving (38) for ζ yields

$$\zeta = -1.52/k = -1.52\lambda/2\pi, \tag{39}$$

i.e., the velocity reverses when the perturbation amplitude ζ is 0.24 of the wavelength.

Numerical Simulations

Two-phase, two-dimensional solidification problems were solved using Succinonitrile and water thermal properties. Succinonitrile was selected because of its ideal thermal properties and extensive physical documentation and testing by Glicksman and co-workers [13–15]. Numeric testing of water was performed because of its obvious physical importance and to introduce effects of anisotropy. Table IV lists the thermal parameters used in the numeric tests for each material and Table V summarizes the numerical test parameters. The domain in Fig. 1 was discretized with 20 proportionally spaced elements perpendicular to the phase front

TABLE IV

Thermal Properties Used for Succinonitrile and Water in the Numerical Simulations

Property	Symbol	Units	Succinonitrile	Water
Thermal conductivity	K	cal/s/cm/ C	5.36×10^{-4} 5.32×10^{-4}	5.38×10^{-3} 1.35×10^{-3}
Volumetric specific heat	c	cal/cm^3/ C	0.470 0.459	0.461 1.007
Volumetric latent heat of fusion	L	cal/cm^3	10.86	73.07
Thermodynamic equilibrium temperature for planar surface	T_m	K	331.24	273.15
Surface energy	γ	cal/cm^2	0.214×10^{-6}	0.695×10^{-6}
Kinetic mobility	μ	cm/s/ C	20	20 A axis 0 C axis

in the liquid region and 4 similarily spaced elements in the solid zone. The discretization along the phase front involved 44 equally spaced elements in both solid and liquid regions. The boundary conditions along Γ are shown in Fig. 1.

For a unit nondimensional undercooling, $\Delta U = \Delta Tc/L = 1$, an arbitrary steady-state background velocity may be selected [3]. We took advantage of this fact for

TABLE V

Test Parameters Used in the Numerical Simulations

Figure	Nodes/λ	Sigma σ	Fourier r	Peclet Pe	Courant Co	Undercooling ΔU
8	10	15	120	2.4E-3	0.29	1.0
9	10	35	300	0.75E-3	0.23	1.0
11	30	12	100	1.E-3	0.1	1.0
13	90	830	7400	0.003E-3	0.023	1.0
14	90	850	26000	0.24E-3	6.0	.25
17	90	300	7500	0.2E-3	1.5	1.0

Note. All tests used: 21 proportionally spaced nodes perpendicular to phase front in the liquid region, 5 similarly spaced nodes perpendicular to phase front in the solid region, the liquid field extended 98% of the thermal range based on $U_L = \exp[-V(x-S)/D] - 1$, the average CPU time was 6 min/time step for a 25×45 grid, nondimensional formulations

$\sigma = \mu(\gamma T_m/L)(\Delta t/\Delta S^2)$, where ΔS is the node spacing along the phase front,

$r = D(\Delta t/\Delta x^2)$, where Δx is the node spacing into the undercooled liquid,

$\mathrm{Pe} = V_x \Delta x/D$,

$\mathrm{Co} = r(\mathrm{Pe})$,

$\Delta U = c\Delta T/L$.

the first series of tests. Consider the test case where Succinonitrile had the following initial conditions;

$$dS/dt = V = 0.01 \text{ cm/s},$$
$$U_l = \exp[-V(x-S)/D] - 1,$$
$$U_s = 0.$$

The neutral stability wavelength predicted via (36) is $\lambda_s = 1.58 \times 10^{-3}$ cm and a fastest growing wavelength of $\lambda_{\max} = 2.74 \times 10^{-3}$ cm. The domain was discretized

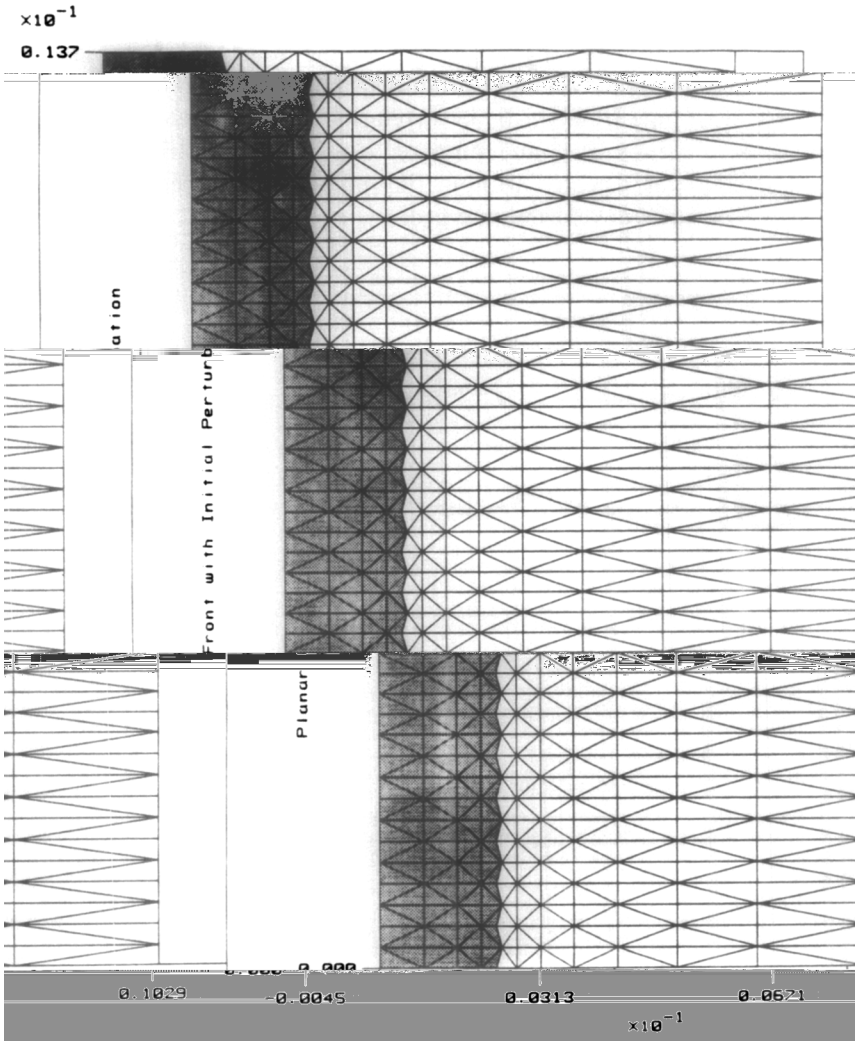

FIG. 7. Finite element grid about phase front showing initial node-to-node perturbation with $\Delta x = \Delta x^{**}$.

with approximately 10 nodes/λ_{max}. A numeric node-to-node perturbation was introduced such that each phase front node had an angle change of $\Delta\alpha^{**}$, Fig. 7. As the test proceeded the numeric perturbation decayed. This node-to-node oscillation crudely represented a wavelength of $\lambda = 0.6 \times 10^{-3}$ cm which is well below λ_s and stable in the continuum. As the front continued to advance into the undercooled melt a longer unstable waveform surfaced, Fig. 8. The average wavelength of this instability was $\lambda = 2.6 \times 10^{-3}$ cm and the fastest growing wave measured $\lambda = 2.8 \times 10^{-3}$ cm, comparable to λ_{max}. The source of this unprovoked disturbance is roundoff error, which can be expected to seed all wavelengths equally. The emergence of $\lambda \sim \lambda_{max}$ as the dominant feature supports the validity of the numerical method. Further verification is found in the evaluation of ω for $\lambda = 2.8 \times 10^{-3}$ cm: 15 s^{-1} via (35) and 17 s^{-1} for the numerical wave via (37).

Increasing the planar front velocity tenfold produces similar results. The numeric perturbations decayed with time while unstable waveforms surfaced with the fastest [redacted] (35), Fig. 9. This test case was repeated without the initial numeric perturbations and similar physically unstable waveforms emerged.

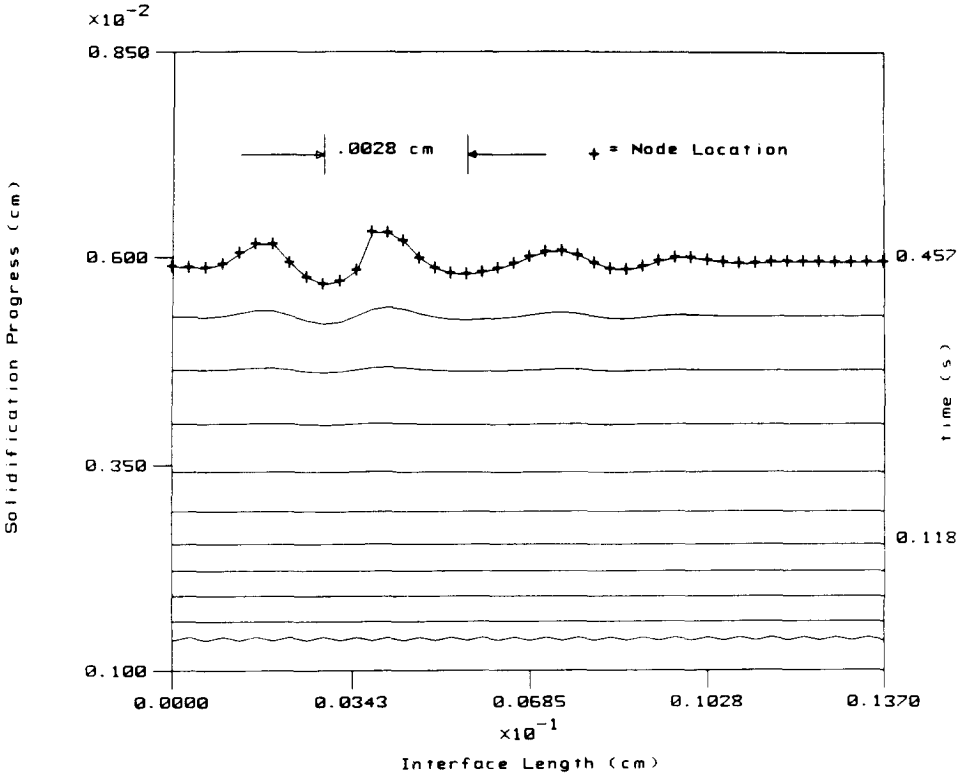

FIG. 8. As solidification front advances the numeric perturbation decays and an unstable waveform surfaces. The background velocity is $V = 0.01$ cm/s and $\lambda_{max} = 2.74 \times 10^{-3}$ cm via Eq. (35). The times shown are for time steps 17 and 41, respectively.

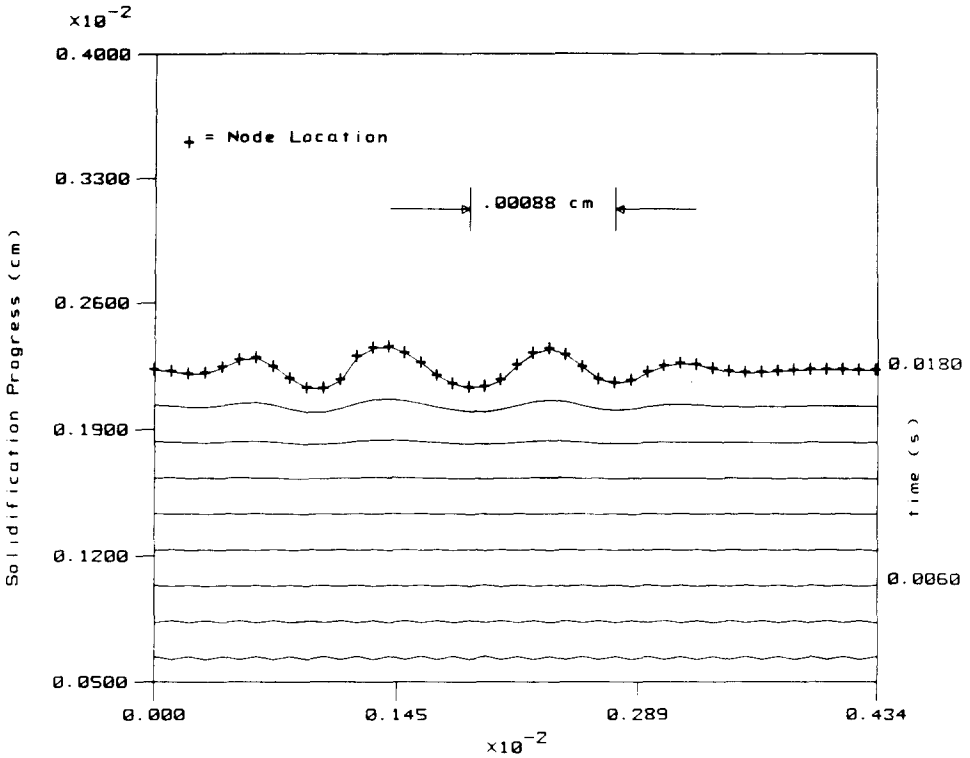

FIG. 9. A tenfold increase in velocity ($V = 0.1$ cm/s) produces $\lambda_{max} = 8.7 \times 10^{-4}$ cm via Eq. (35). The times shown are for time steps 3 and 9, respectively.

The above experiments were performed with symmetry boundary conditions applied on both sides of the phase front, and thus only support harmonics of the fundamental wavelength that is twice the boundary length. To ensure that the onset and growth of the observed numeric wavelengths were not dictated by the boundary conditions, the phase front length and node spacing were set to allow numerous wavelengths in the physically unstable range. A Fourier decomposition of Fig. 8 was performed which clearly shows the available wavelengths and the wavelength migration of the spectrum toward the harmonic closest to that corresponding to λ_{max}, Fig. 10a–d.

FIG. 10. Top graph shows perturbations from the average phase front along the interface. The lower graph is a Fourier decomposition of the interface showing the Fourier coefficient magnitude of each available wavelength given the symmetry boundary conditions of the interface. The wavelengths are represented as harmonics of the wavelength that is twice the boundary length. (a) At time $t = 0.002$ s, the Nyquist frequency is dominant ($\lambda/\Delta x = 2$). (b) At time $t = 0.023$ s, the interface has returned to a planar front and all Fourier coefficients are small. (c) Unprovoked wavelengths are emerging at time $t = 0.127$ s. Equation (35) predicts stable wavelengths for $\lambda < \lambda_S$ ($= 1.58 \times 10^{-3}$ cm) or for harmonics ≥ 18. (d) The largest Fourier coefficient at $t = 0.295$ s corresponds to $\lambda_{max} = 2.74 \times 10^{-3}$ cm.

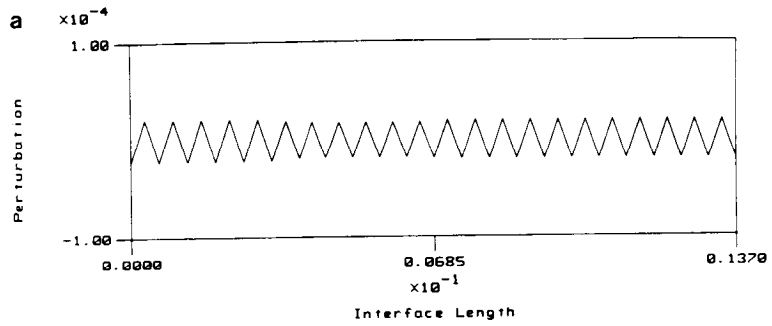
a
x10^-4
1.00
-1.00
Perturbation
0.0000
0.0685
0.1370
x10^-1
Interface Length

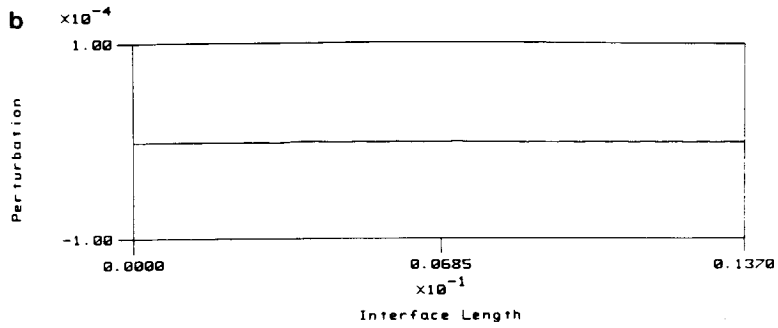
b
x10^-4
1.00
-1.00
Perturbation
0.0000
0.0685
0.1370
x10^-1
Interface Length

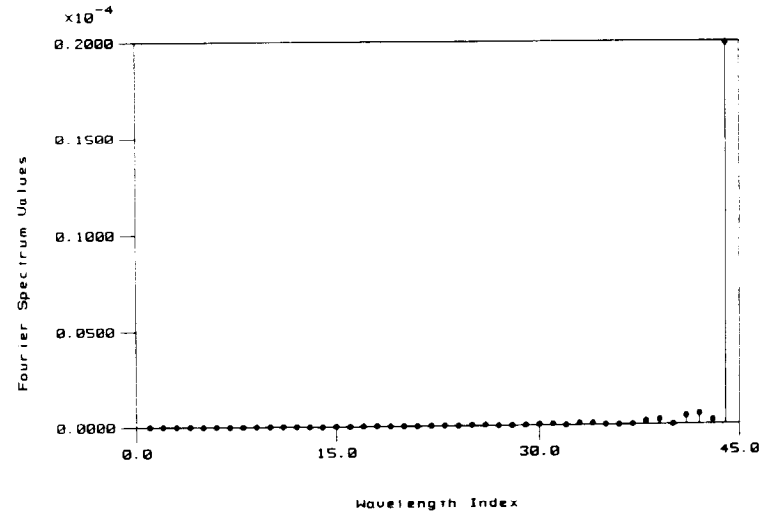
x10^-4
0.2000
0.1500
0.1000
0.0500
0.0000
Fourier Spectrum Values
0.0
15.0
30.0
45.0
Wavelength Index

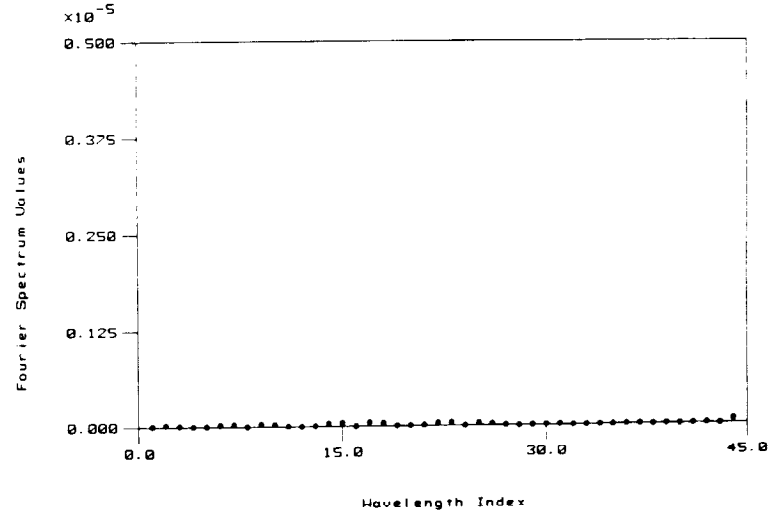
x10^-5
0.500
0.375
0.250
0.125
0.000
Fourier Spectrum Values
0.0
15.0
30.0
45.0
Wavelength Index

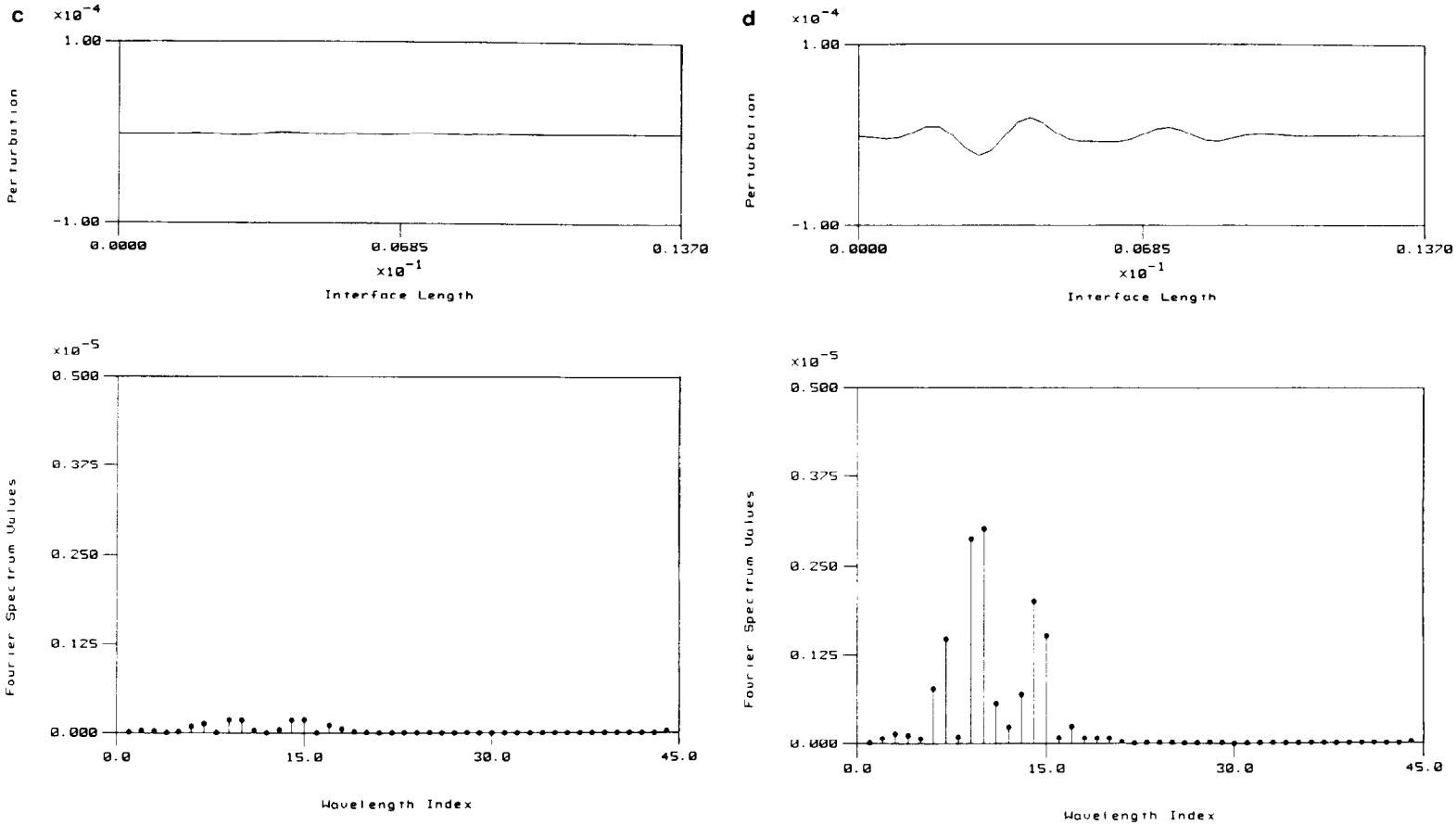
c
x10^-4
1.00
-1.00
Perturbation
0.0000
0.0685
0.1370
x10^-1
Interface Length
d
x10^-4
1.00
-1.00
Perturbation
0.0000
0.0685
0.1370
x10^-1
Interface Length
x10^-5
0.500
0.375
0.250
0.125
0.000
Fourier Spectrum Values
0.0
15.0
30.0
45.0
Wavelength Index
x10^-5
0.500
0.375
0.250
0.125
0.000
Fourier Spectrum Values
0.0
15.0
30.0
45.0
Wavelength Index

The following test demonstrated the robustness of the deforming mesh technique. The initial thermal conditions of Fig. 8 were repeated on a grid discretized with 30 nodes/λ_{max} and a boundary length of $3\lambda_{max}$. The resolution perpendicular to the front remained unchanged. A small perturbation $x = x_0 + \zeta_0 \cos(2\pi y/\lambda_{max})$ was used to seed the simulation. Figure 11a shows the development and growth of this unstable waveform as a function of time with the initial and final grid deformations shown in Figs. 11b, c, respectively. The thermal profile at the end of the simulation shows that the temperature disturbance due to the perturbations is limited to a

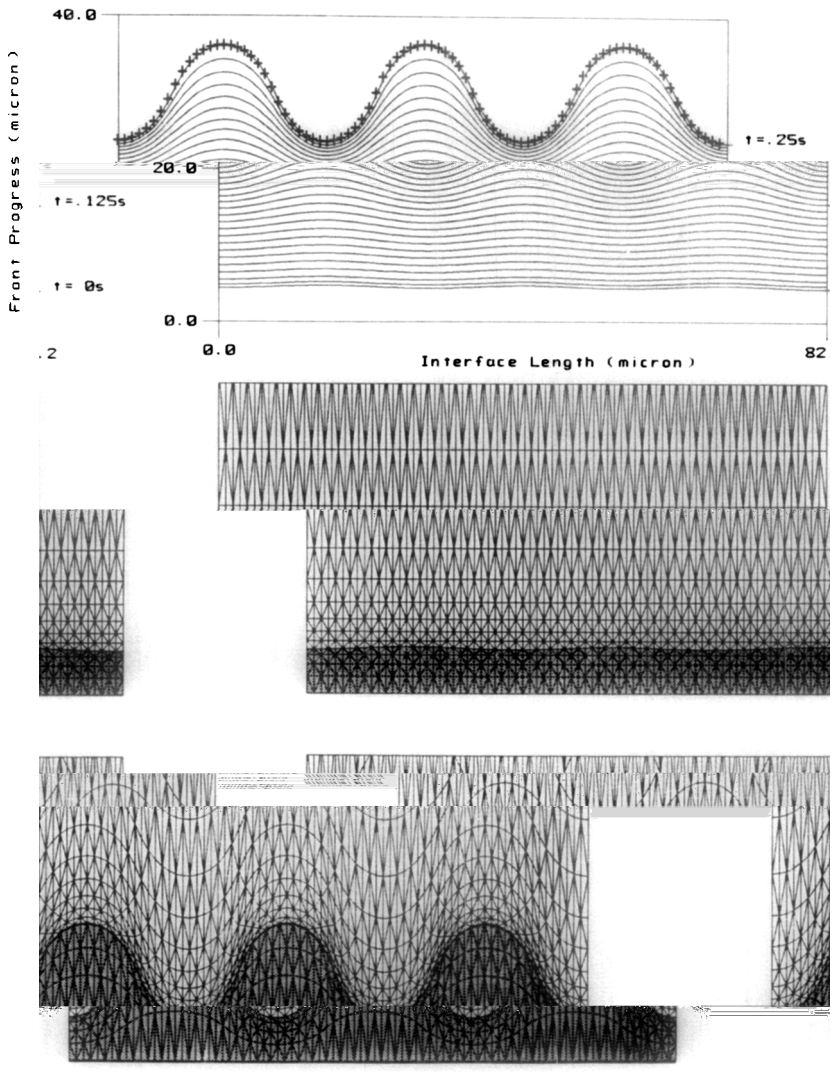

FIG. 11. (a) Development and growth of λ_{max}. (b) Initial grid deformation in the vicinity of the interface. (c) Final grid deformation in the vicinity of the interface at time $= 0.25$ s.

range of a few λ_{max}; and that the zero isotherm intersects the interface where $\mathbb{C} \approx 0$, Fig. 12.

In the above simulations the numeric system became unstable as the perturbation length ζ approached $0.2\lambda_{max}$. We increased the phase front resolution to 90 nodes/λ_{max} and performed tests using the first test-case paremeters with a boundary length of $\lambda_{max}/2$. The node resolution perpendicular to the planar front remained unchanged. As the interface advanced the unstable waveform λ_{max} grew in amplitude, Fig. 13. However, the numeric system became unstable at approximately the same ζ/λ ratio of 0.2. The instability manifested itself approximately $1R$ behind the waveform tip where R is the tip radius of curvature. We note from Huang and Glicksman [14] that sidebranching emerged at approximately $1.2R$ behind the (r, z) dendrite tip over a wide range of undercooling. Unfortunately, our current

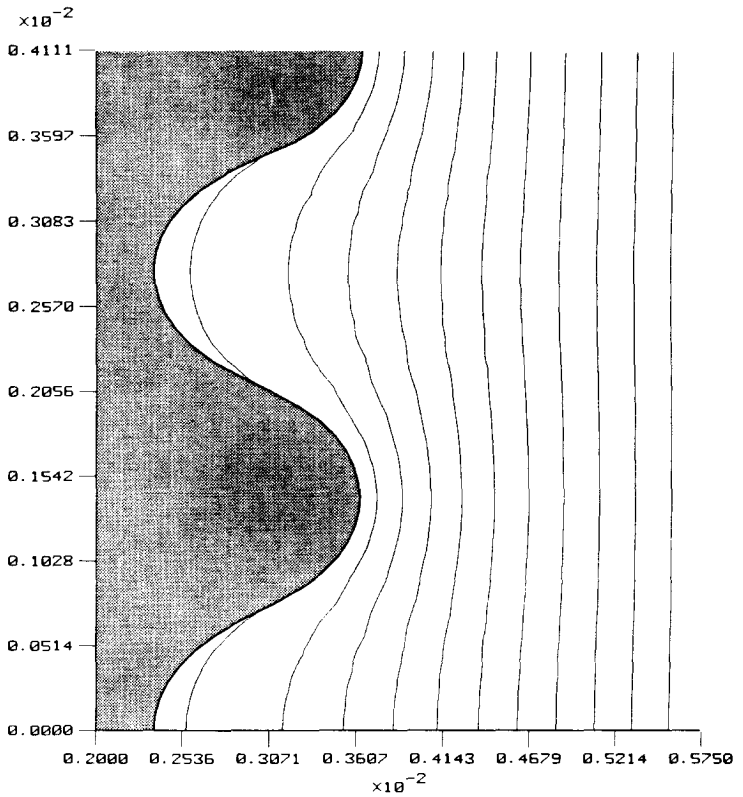

FIG. 12. Thermal contour bands in the undercooled liquid range from $U = 0$ to $U = -0.02$ in equal temperature increments where U is the nondimensional temperature. The shaded zone is the solid and the isotherm values drop as the distance into the undercooled liquid increases. Only the lower half of the interface is shown for clarity. Note that the zero isotherm intersects the interface where $C \approx 0$ and that hot spots have formed in the "valleys" of the interface.

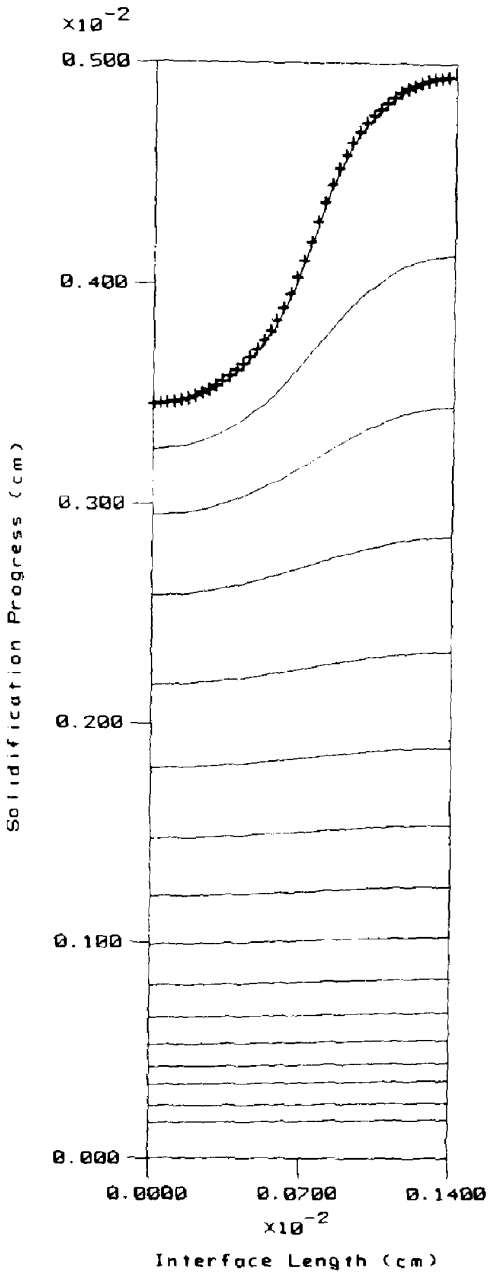

FIG. 13. The node resolution is increased to 90 nodes/wavelength to study interface stability as a function of ζ/λ.

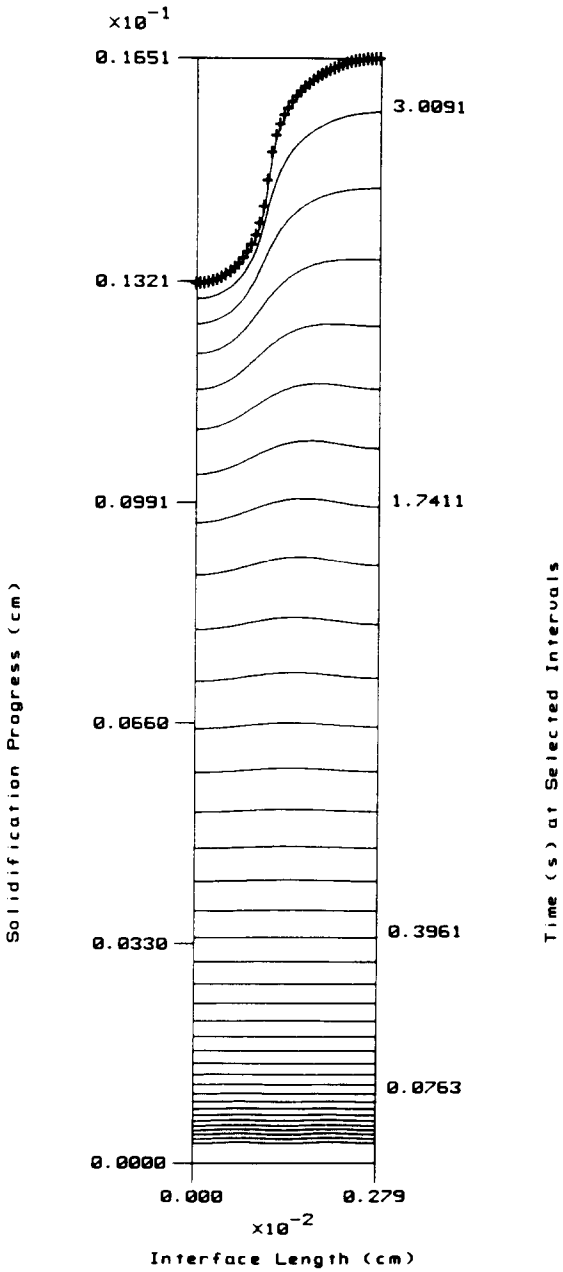

FIG. 14. The evolution and decay of several waveforms is recorded during the transient planar simulation with $\Delta U = 0.25$.

planar (x, y) model allows no y motion such that the waveform cannot realign itself to simulate a sidebranch. In a future paper we will address this issue.

For $\Delta U \neq 1$ there is no steady-state planar front velocity. However, the continuum stability analysis remains valid for the transient situation as mentioned previously. Consider the test case where $\Delta U = 0.25$ with an initial velocity of $V = 0.02$ cm/s and a small amplitude waveform $\lambda = 1.4 \times 10^{-3}$ cm $= 1.2\lambda_s$. Initially, the average front velocity decreased with time. Consequently, λ_s increased such that the initial waveform became stable and the numerical results show the phase front returned to a planar front. As the front progressed a new longer waveform emerged with $\lambda = 2.8 \times 10^{-3}$ cm. The average front velocity at the onset of this waveform shows that waveform to be in the unstable region. This waveform propagated for a period of time and then transformed into another still longer waveform

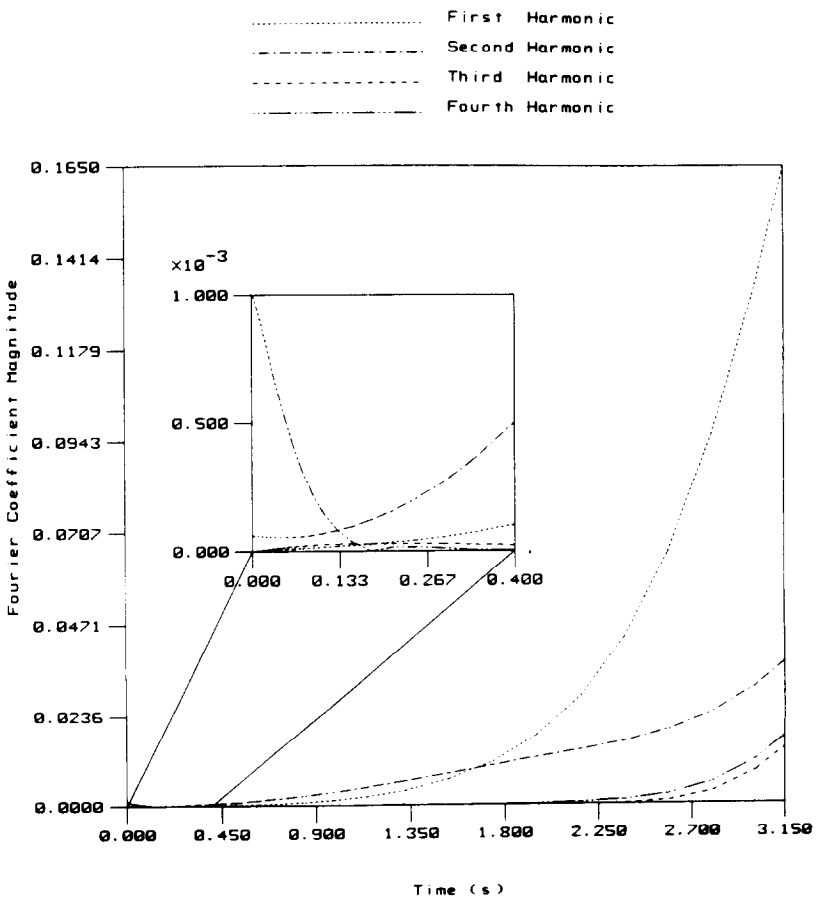

FIG. 15. The Fourier coefficients of the waveforms shown in Fig. 14 are plotted as a function of time. The exponential growth rate of the unstable waveforms is in complete agreement with the stability

($\lambda = 5.6 \times 10^{-3}$ cm) as the front velocity continued to decay with time, Fig. 14. The interface was Fourier decomposed and the magnitudes of the first 4 harmonics plotted as a function of time, Fig. 15. The exponential growth of the most unstable waveforms is in complete agreement with that predicted via the stability analysis. In Fig. 16, λ_s and λ_{max} via (35) are shown as a function of time based on the average front velocity. The dominant numeric waveform is that closest to λ_{max} throughout the simulation, as expected, Fig. 16.

The phase-front velocity in (2d) is a function of mobility, μ, which was treated as a constant for Succinonitrile. However, the nonisotropic nature of water at small undercoolings is a function of the large interfacial kinetic differences between the A axis and C axis growth planes. A strong preference for growth in the basal plane along the A axis exists compared to that perpendicular to the basal plane,

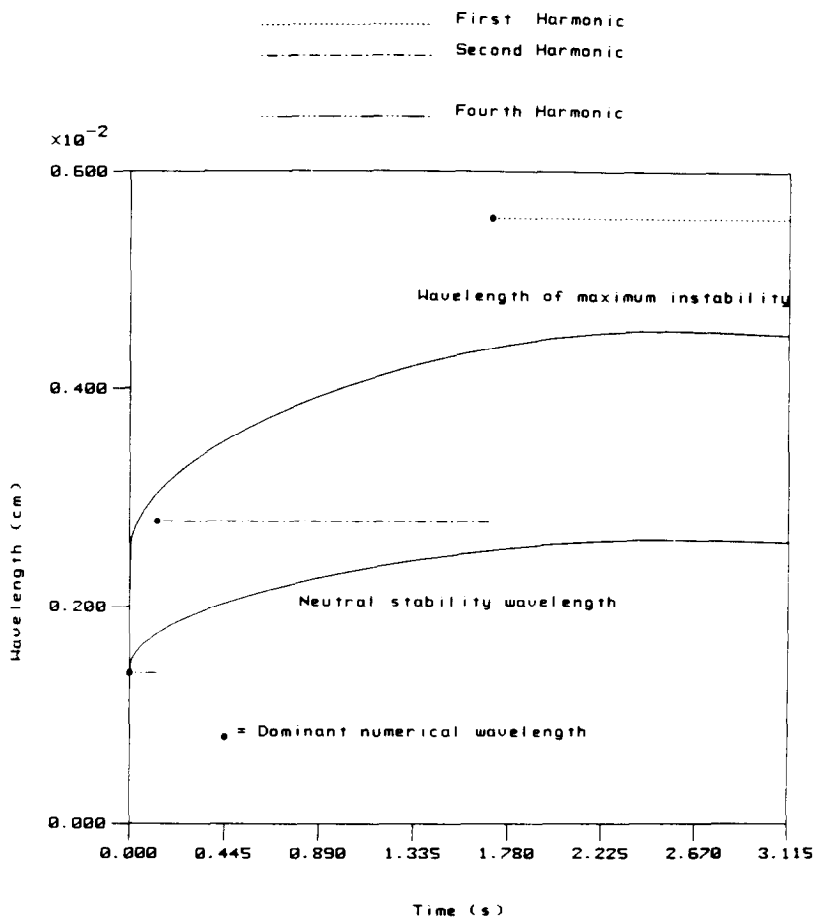

FIG. 16. The dominant numeric waveform is that closest to λ_{max} throughout the transient simulation.

the C axis. Consequently, the mobility is a function of position which we described as a function of its A axis orientation, i.e.,

$$\mu(x, y) = \cos(\alpha)\, \mu_{\alpha=0}, \tag{40}$$

where the x, y orientation corresponds to the A, C planes of ice, respectively, and the mobility in the C plane is taken as zero. Two test simulations were performed

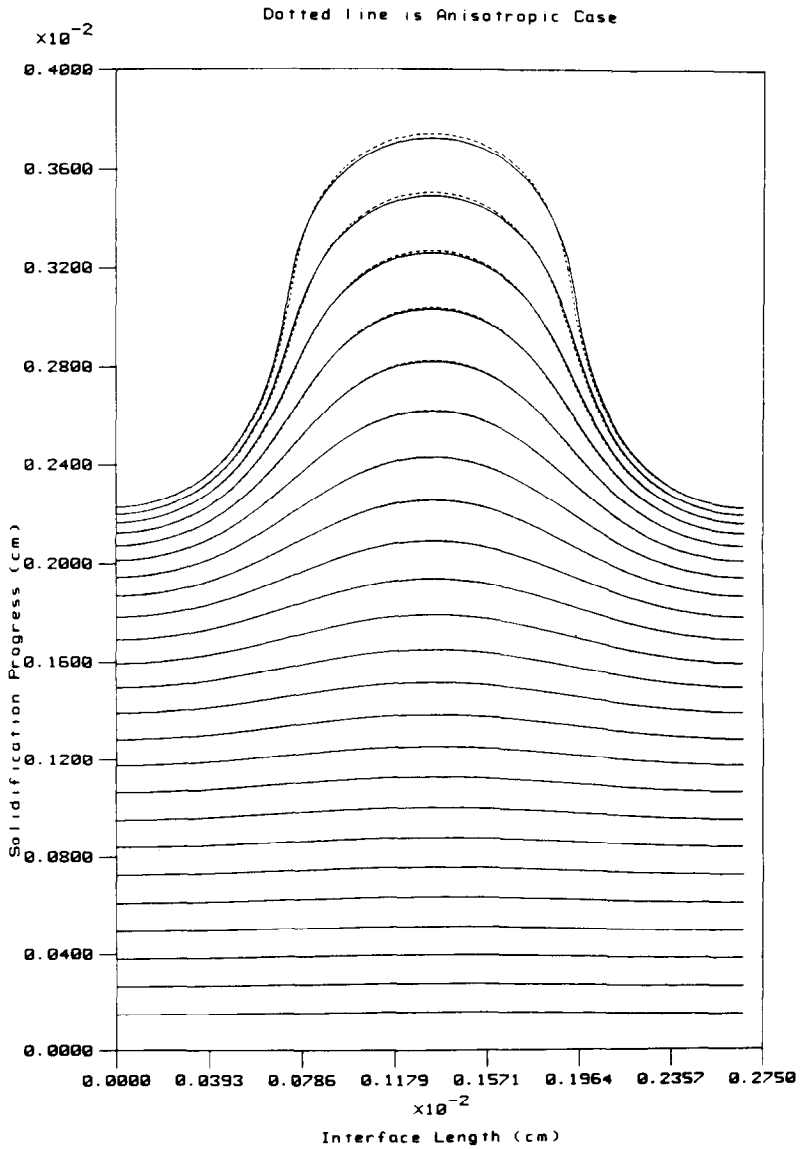

FIG. 17. The anisotropic interface shape becomes elongated relative to that in the isotropic test only after significant portions of the interface are orientated in the nongrowth direction, i.e., the C-axis.

using water thermal properties and an initial x-velocity of 0.01 cm/s. The first test used an isotropic mobility whereas the second case used (40). The anisotropic results are identical to the isotropic case when the normal direction coincides with the x-direction. After the waveform amplitude became significant however, the anisotropic shape was elongated compared to that of the isotropic simulation, Fig. 17. However, the actual volume of ice formed was somewhat less in the anisotropic case, as expected. Since in the current calculations we restrict y motion, the isotropic V_x is expressed as:

$$V_x = (\mu/\cos\alpha)[(-\gamma T_m/L)\,\mathbb{C} - T] \tag{41}$$

with μ constant, whereas, the anisotropic V_x is

$$V_x = \mu_{\alpha=0}[(-\gamma T_m/L)\,\mathbb{C} - T]. \tag{42}$$

Consequently, for the same thermal field and curvature the isotropic velocity is greater than or equal to the anisotropic velocity.

Summary and Conclusions

Two-dimensional finite element solutions for planar solidification from an undercooled melt were presented. The stability analysis of the planar front presented by Langer [3] is valid for transient situations and provides an excellent basis for model testing. The numeric simulations showed the decay of stable disturbances as well as the onset and propagation of unstable numerical waveforms which reproduced those predicted in the continuum analysis with fidelity. The inherent instabilities associated with the freezing process required a more comprehensive treatment of the interfacial temperature than that specified in stable Stefan-type problems. Radiation-type boundary conditions on the interface that incorporated temperature effects associated with curvature and interfacial kinetics were necessary. The interfacial temperature depression due to curvature is the primary restraining factor during dendritic growth. However, the numerical curvature formulation has discretization limits for stability and was treated implicitly within the thermal iteration and within the time step to overcome severe time-step constraints imposed on explicit curvature expressions. The numeric simulations of anisotropic ice showed similar waveforms patterns at the onset of the instability to those of isotropic cases. However, as the amplitude of the waveform increased significant lengths of interface became orientated along the C axis where interfacial kinetics inhibit growth. This altered the interface shape by elongating the dendrite finger.

We are currently expanding these formulations to investigate sidebranching and solute effects. Along these lines we note that Ungar and Brown [16–18] are developing related finite element techniques to model the evolution of dendrites in multi-component alloys. Their work concentrates on solute diffusion with a fixed thermal field imposed. While their numerical formulations are different from those presented here, they also noted the need to treat the location of the interface implicitly to avoid time step constraints. We believe our results in the thermal

domain complement their solute findings and that our stability analysis of the interface may be applicable to their system.

Appendix

The amplification rate (35) obtained by Langer [3] is easily obtained without the assumptions of a steady-state, unit undercooling in the melt at infinity. The key is the expression of the background temperature field T_B in the melt in a Taylor series. The first derivative may be obtained from the latent heat balance:

$$(\partial T_B/\partial x)|_S = -LV/K, \tag{A1}$$

where V is the background velocity and x is the direction of growth as in Fig. 1. The second derivative is available from the heat equation:

$$(\partial^2 T/\partial x^2) = (1/D)(\partial T/\partial t - V\partial T/\partial x), \tag{A2}$$

where x is assumed fixed to the moving front. Since the background situation is a planar front, curvature is zero and T_B is constant at $x = 0$,

$$(\partial^2 T_B/\partial x^2)|_S = -(V/D)\,\partial T_B/\partial x = V^2 L/(DK). \tag{A3}$$

Thus the background distribution of T and $\partial T/\partial x$ at any point in time is, to first order,

$$T_B = -(LV/K)\,x, \tag{A4}$$

$$(K\partial T_B/\partial x) = -LV + (LV^2/D)\,x. \tag{A5}$$

Add the perturbation $T_0 \exp(iky - qx + \omega t)$ and $\zeta_0 \exp(iky + \omega t)$ to the temperature and boundary position, with q given by (34). Satisfaction of temperature boundary condition (33) to first order yields, with the help of (A4), the temperature perturbation amplitudes in both phases:

$$T_0^L = \zeta_0[LV/K - k^2\gamma T_m/L], \tag{A6}$$

$$T_0^S = \zeta_0[k^2\gamma T_m/L]. \tag{A7}$$

Equation (A5) may then be utilized in the latent heat balance at $x = \zeta$, and the amplification rate (35) is obtained to first order.

Acknowledgments

We wish to acknowledge the helpful conversations with Steven Daly, Research Engineer at U.S. Army Cold Regions Research and Engineering Laboratory and Professor Harold Frost, Thayer School of Engineering. This work has been supported by the U.S. Army Cold Regions Research and Engineering Laboratory under Contract DACA 89-84-K-0002; by the National Science Foundation under Grant CEE-8352226; and by the General Electric Company.

REFERENCES

1. W. W. MULLINS AND R. F. SEKERKA, *J. Appl. Phys.* **35** (1964), 444.
2. R. F. SEKERKA, "Morphological stability," *Crystal Growth: An Introduction*, edited by P. Hartman (North–Holland, Amsterdam, 1973).
3. J. S. LANGER, *Rev. Modern Phys.* **52** (1980), 1.
4. J. M. SULLIVAN, JR., D. R. LYNCH, AND K. O'NEILL, in *NUMETA'85*, edited by J. Middleton and G. N. Pande (A. A. Balkema, 1985), p. 527.
5. J. W. CAHN, W. B. HILLIG, AND G. W. SEARS, *Acta Metal.* **12** (1964), 1421.
6. D. R. LYNCH AND K. O'NEILL, *Int. J. Numer. Methods Eng.* **17** (1981), 81.
7. K. O'NEILL AND D. R. LYNCH, "A finite element solution for freezing problems, using a continuously deforming coordinate system," *Numerical Methods in Heat Transfer*, edited by Lewis *et al.* (Wiley, New York, 1981), Chap. 11.
8. D. R. LYNCH, *J. Comput. Phys.* **47** (1982), 387.
9. D. R. LYNCH AND J. M. SULLIVAN, JR., *J. Comput. Phys.* **57** (1985), 303.
10. M. R. ALBERT AND K. O'NEILL, *Int. J. Numer. Methods Eng.* **23** (1986), 591.
11. G. D. SMITH, "Convergence, Stability and Consistency," *Numerical Solution of Partial Differential Equations; Finite Difference Methods*, (Clarendon, Oxford Univ. Press, London, 1978), Chap. 3.
12. J. P. KALLUNGAL AND A. J. BARDUHN, *AIChE J.* **23** (1977), 294.
13. S.-C. HUANG AND M. E. GLICKSMAN, *Acta Metal.* **29** (1981), 701.
14. S.-C. HUANG AND M. E. GLICKSMAN, *Acta Metal.* **29** (1981), 717.
15. M. E. GLICKSMAN, R. J. SCHAEFER AND J. D. AYERS, *Metal. Trans. A* **7** (1976), 1747.
16. L. H. UNGAR, M. J. BENNETT, AND R. A. BROWN, *Phys. Rev. B* **31** (1985), 5923.
17. L. H. UNGAR AND R. A. BROWN, *Phys. Rev. B* **31** (1985), 5931.
18. L. H. UNGAR AND R. A. BROWN, *J. Comput. Phys.*, submitted.